INFLUENCE OF TURBULENCE MODELS IN THE PREDICTION OF CAVITATION OCCURRENCE

A. Evangelisti [(1)] – *G. Agati* [(1)] – *H. Haghighifard* [(1)] – *F. Rispoli* [(1)] – *P. Venturini* [(1)] – *D. Borello* [(1)]

[(1)] Department of Mechanical and Aerospace Engineering
Sapienza, University of Rome
Rome, Italy
adriano.evangelisti@uniroma1.it
giuliano.agati@uniroma1.it
haghighifard.1915876@studenti.uniroma1.it
franco.rispoli@uniroma1.it
paolo.venturini@uniroma1.it
domenico.borello@uniroma1.it

ABSTRACT

In the present paper the effect of turbulence models on cavitation occurrence is evaluated by means of numerical simulations on a NACA 66 (MOD) profile. Cavitation will be assessed through the employment of the widely applied Singhal model, based on the use of the Rayleigh-Plesset equation for bubble dynamics description. Two different turbulence models are used to assess the effect of turbulence on cavitation. For this purpose, Scale Adaptive Simulations (SASs) and Transitional Shear Stress Transport (TSST) simulations are carried out on the NACA test case. Results are discussed for two distinct cavitation numbers comparing experimental data and simulations-obtained values of the non-dimensional pressure coefficients. Moreover, temporal trends and Fast Fourier Transformations (FFTs) will be evaluated for the physical quantities of interest, highlighting the main turbulence-induced fluctuating modes. A direct visualization of the cavity breathing phenomenon is then proposed for the severer cavitating condition case.

KEYWORDS

CAVITATION, CFD, SAS, TSST, BUBBLE DYMANICS

NOMENCLATURE

Latin symbols

C	Mass transfer coefficient	(m/s)
C_p	Pressure coefficient	(-)
f	Mass fraction	(-)
k	Turbulent kinetic energy	(J/kg)
m_B	Bubble mass	(kg)
n_B	Bubble number	(-)
p	Static pressure	(Pa)

Abbreviations

CFL	Courant Friedrichs Lewy
EXP	Experimental data
FFT	Fast Fourier Transformation
NCG	Non-condensable gas
LHS	Left-hand side
RHS	Right-hand side
SAS	Scale Adaptive Simulation

R_B	Bubble radius	(m)
t	Time	(s)
v	Flow velocity	(m/s)
V_B	Bubble volume	(m^3)
V_C	Cavity volume	(m^3)

TSST	Transitional Shear Stress Transport

Greek symbols

α	Vapour volume fraction	(-)
β	Liquid volume fraction	(-)
γ	Water surface tension	(N/m)
μ	Dynamic viscosity	(Pa s)
ν	Kinematic viscosity	(m^2/s)
ρ	Volumetric mass	(kg/m^3)
σ	Cavitation number	(-)
ψ	Net volumetric mass rate	(kg/(m^3s))

Subscripts

c	Condensation process
e	Evapouration process
j	Non condensable gaseous species
l	Liquid water
ref	Reference conditions
v	Vapour water
x, y, z	Cartesian conditions
τ	Turbulent variables
0	Equilibrium conditions
∞	Far field conditions

INTRODUCTION

When the liquid stream static pressure drops below the saturated vapour pressure, a physical local-state transition from liquid to vapour occurs, Young (1999). This event leads to micro-structured gaseous bubbles enucleations that, transported by the surrounding liquid phase to higher head zones, undergo a sharp implosion, Gohil and Saini (2014). The whole phenomenon is named cavitation. Once the bubbles implode, liquid jets form and may hit a surrounding wall provoking cavitation erosion, Dular et al. (2006). Cavitation is a very common phenomenon in fluid machinery. Significant hydrostatic head reduction is often encountered over the anterior zone of a pump wheel or the rear part of a turbine blade. These are the regions where the risk of cavitation occurrence result to be more pronounced. For this reason, to counteract the cavitation damage effect, inducers or coated materials are frequently adopted in pumps and turbines, respectively, Hong et al. (2021).

Over the past years, several approaches were developed to model cavitation phenomena: among the conducted studies, many engineering applications are based on the use of homogeneous mixture models, easy to be employed in large-scale cavitation cases, Ghahramani et al. (2021). They are further divided into two groups: barotropic state equation-based models and transport equation models, Savio et al. (2021). The former is properly adapted to describe the choke effect on the flow rate but its greater lack is about a proper prediction of cavitation dynamics under turbulent flow conditions, Ducoin et al. (2012). Transport equation models are the most used since they allow direct quantification of the net mass transfer rate when computing source and sink terms, which act as the accelerator and decelerator of the cavitation process, respectively. Models developed by Merkle (1998) and Kunz et al. (2000) strictly relate source terms of the transport equation to the density field variation, which is proportional to the dynamic pressure one. Saito et al. (2007) model results to be especially suited to evaluate the cavitation source terms in the case of plane surfaces. Instead, when mass and momentum equations need to be evaluated at the interphase, the implementation of the model of Senocak and Shyy (2002) results to be more suitable. Finally, Singhal et al. (2002), Zwart et al. (2004) and Schnerr and Sauer (2001) models deserve to be discussed separately. In fact, they base the evaluation of the source terms on the Rayleigh-Plesset bubble dynamics equation. Their novelty is in the computation of the net interphase mass transfer rate through the definition of a bubble number density.

Bubble dynamics-based equation models are particularly appropriate for the description of cavitating flows around marine propellers, hydro turbines, or water pumps. Their mathematical structure highlights straightforward management of the principal cavitating flow parameters. Lee et al. (2021) compared the Schnerr and Sauer (2001) model with that of Merkle (1998), showing a better fit with the experimental results in the case of a cavitating flow around a NACA 66 hydrofoil marine propeller. Morgut et al. (2018), proved a good agreement of the Zwart et al. (2004) model when upgrading the turbulence modelling from a Reynolds Averaged Navier Stokes (RANS) simulation to a Scale Adaptive Simulation (SAS) for both a marine propeller and a Kaplan turbine. Cavitation patterns are mainly influenced by geometry and flow conditions. To approach the real-experimental set-up features, models should be calibrated through the determination of numerical coefficients in order to optimize their application and validation, Morgut et al. (2018) and Bilus et al. (2013).

The cavitation number derived from Thoma's considerations, Kumar and Saini (2010), is widely used to compare cavitating behaviour of fluid machinery.

$$\sigma = \frac{p_\infty - p_v}{\frac{1}{2}\rho v_\infty^2} \tag{1}$$

In the present paper, the effect of different turbulence models on cavitation is evaluated. Their prediction reliability is tested on a two-dimensional NACA 66 (MOD) profile for which experimental data are available from the work of Shen and Dimotakis (1989).

CAVITATION MODEL

The most widespread and employed cavitation models are all based on the bubble dynamics, whose description was elaborated by Rayleigh-Plesset, Young (1999). Cavitation models are composed of two complementary terms, i.e., the formation and disappearance rates, both derived from considerations carried out about the continuity phases equations and the growing velocity of the vapour bubbles. The assessment of this second aspect strongly relies on the well-known Ryleigh-Plesset equation:

$$\frac{p_v(t) - p_\infty(t)}{\rho_l} = R_B \frac{d^2 R_B}{dt^2} + \frac{3}{2}\left(\frac{dR_B}{dt}\right)^2 + \frac{4\nu_l}{R_B}\frac{dR_B}{dt} + \frac{2\gamma}{\rho_l R_B} \tag{2}$$

To simplify the management of eq. (2), a *first order approximation* is often applied in calculating the radius velocity term. As stated by Berntsen et al. (2001), viscous, surface tension and second derivative order terms in the RHS of eq. (2) have always a negligible order of magnitude, so they can be neglected:

$$\frac{dR_B}{dt} = \sqrt{\frac{2}{3}\frac{p_v(t) - p_\infty(t)}{\rho_l}} \tag{3}$$

The analytical form of the bubble radius velocity during the condensation stage is quite complex for models' implementations. For this reason, in bubble dynamics-based cavitation models eq. (3) is also applied during the imploding stage. The introduced error is taken into account by proper calibrating two different numerical coefficients for the evapouration and condensation terms evaluation. Among the bubble dynamics-based models, the Singhal one is mentioned in the literature as the full cavitation model thanks to its capacity to capture the greatest number of cavitation aspects.

It allows for a direct consideration of turbulence and provide an extension to other non-condensable gas species. These characteristics give to the Singhal cavitation model a high level of applicability, above all when turbulent flow conditions need to be investigated.

For these reasons, it will be applied in conjunction with TSST and SAS turbulent models, for turbulent assessments. Starting from liquid and vapour continuity equations it is possible to explicit the role of the net volumetric mass rate ψ , Kozubková et al. (2012):

$$\frac{\partial}{\partial t}\left[(1-\alpha)\rho_l\right]+\vec{\nabla}\cdot\left[(1-\alpha)\rho_l\vec{v}\right]=-\psi \tag{4}$$

$$\frac{\partial}{\partial t}\left(\alpha\,\rho_v\right)+\vec{\nabla}\cdot\left(\alpha\,\rho_v\,\vec{v}\right)=\psi \tag{5}$$

$$\psi=\psi_e-\psi_c \tag{6}$$

Where $\alpha=\left(\rho-\rho_l\right)/\left(\rho_v-\rho_l\right)$.

To determine a relation for ψ, which identifies quantitatively the cavitation phenomenon inside the liquid current, it is possible to combine together eq. (4) and (5) in order to recast a general form of the cavitation model:

$$\psi=\frac{\rho_l\rho_v}{\rho}\frac{d\alpha}{dt} \tag{9}$$

To characterize the model, an expression for the vapour volume fraction is needed in order to connect the mass transfer phenomenon to the bubble dynamics geometrical variations. According to the hypothesis of Singhal et al. (2002), the vapour volume fraction is expressed as:

$$\alpha=n_B V_B=\frac{4}{3}\pi n_B R_B^3 \tag{10}$$

From which the general equation form is:

$$\psi=\frac{3\alpha}{R_B}\frac{\rho_l\rho_v}{\rho}\sqrt{\frac{2}{3}\frac{p_v-p_\infty}{\rho_l}} \tag{12}$$

As pointed out by Olsson M. (2008), the radius dependence in eq. (12) can be substituted introducing thermophysical and turbulent flow properties. It has been noted empirically that, during a mass transfer process the mass transfer rate is directly proportional to the donor phase, i.e., during an evapouration process the mass transfer will depend on the liquid volume fraction, conversely during a condensation the mass transfer rate will be affected by the vapour volume fraction. Other assumptions empirically proved by the model's authors aim to extend the cavitation prediction to other non-condensable species, with a deeper investigation about the turbulent kinetic energy treatment. Then, the final form of the Singhal cavitation model, taking into account all the introduced contributions, is:

$$\text{if } p_v \geq p_\infty: \quad \psi_e=C_e\frac{\max\left(1,0;\sqrt{k}\right)}{\gamma}\rho_l\rho_v\sqrt{\frac{2}{3}\frac{p_{v,\tau}-p_\infty}{\rho_l}}\left(1-f_v-\sum_j f_j\right) \tag{13}$$

$$\text{if } p_v < p_\infty : \quad \psi_c = C_c \frac{\max\left(1,0;\sqrt{k}\right)}{\gamma} \rho_l^2 \sqrt{\frac{2}{3}\frac{p_\infty - p_{v,\tau}}{\rho_l}}\, f_v \tag{14}$$

In the Singhal model final structure, vapour volume fractions are often substituted by mass fraction-dependent expressions.

TURBULENCE MODELS

Steady simulations are run making use of the TSST turbulence model. Such a model was selected for its capacity to expand upon the SST *k-ω* model by adding two other transport equations, one for the intermittency and another for the transition onset criteria, expressed as function of momentum-thickness Reynolds number. The model ability in individuating the transition onset relies on the empirical correlations and further improvements developed by Menter et al. (2004). Unsteady simulations, instead, are based on the implementation of the SAS turbulence model. Its hybrid nature allows for direct combination of LES and U-RANS mathematical formulations in exploring the perturbation-induced phenomena on cavitating flows, Hidalgo et al. (2019).

The SAS approach is based on the introduction of the von Kármán length-scale into the turbulence scale equation. The information provided by the von Kármán length-scale allows SAS models to dynamically adjust to resolve structures in a U-RANS simulation, which results in an LES-like behaviour in unsteady regions of the flow field. At the same time, the model provides standard RANS capabilities in stable flow regions. Transport equations of SAS model differs substantially from that of TSST steady formulation by the additional source term for the turbulence eddy frequency, as described by Menter and Egorov (2010). For this reason, the unsteady flow field is initialized starting from the steady converged solution obtained from TSST turbulence model application.

COMPUTATIONAL DETAILS

Simulations are performed through the use of ANSYS Fluent, v21R2. The steady TSST computations are carried out and their converged flow field solutions are used to initialize the unsteady SAS simulations. Both TSST and SAS simulations have the same numerical setup, characterized by a SIMPLEC scheme for pressure – velocity coupling, first order upwind scheme for spatial discretization of density, vapour fraction, turbulent kinetic energy, energy and dissipation rate. Pressure spatial discretization is realized by selecting the PRESTO! scheme, while for the momentum a second order upwind scheme is adopted. For SAS simulations, temporal discretization is carried out through the bounded second order implicit method. Variable CFL-based time steps are adopted by setting the Courant number *Co* = 20 until converged time steps are reached. The explored cavitation conditions are described by σ = 1.76 and σ = 0.91, resulting in an outlet pressure equal to 137.287 kPa and 72.550 kPa, respectively. While a pressure condition is adopted at the outlet (red surface in Fig.1a), at the inlet (blue surface in Fig.1a) a reference velocity equal to 12.36 m/s is set. The Reynolds number based on inlet velocity and chord length is 2.00E+06. Periodical boundary conditions are used for the lateral surfaces (coloured in green in Fig.1a), symmetry boundary conditions are applied on the top and bottom surfaces (coloured in grey in Fig.1a) while adiabatic no-slip wall conditions are adopted for the hydrofoil walls (outlined by black edges in the centre of Fig.1a). A constant temperature of 298 K is considered during simulations, with a corresponding saturation pressure of 3200 Pa and a water liquid density of 997.7 kg/m^3. Trapped air amount, i.e., non-condensable gaseous (NCG) mass fraction, is left equal to the default value, 1.50E-05 (15 ppm). Converged time step sizes are equal to 3.62E-06 s and 3.54E-06 s for σ = 1.76 and σ = 0.91, respectively.

The domain reproduces the NACA 66 (MOD) test case of Shen and Dimotakis (1989). The hydrofoil is characterized by a chord length of 0.15 m and an angle of attack of 4°. The domain geometry is rectangular, with dimension 1.0×0.5 m for the 2D case and 1.0×0.5×0.14 m for the 3D. The computational mesh shown in Fig.1b is composed of a structured layer surrounding the hydrofoil profile (for the boundary layer treatment) and a non-structured buffer to decuple the external and the boundary layer regions. y^+ values computed from converged solutions are well below 10, representing a good compromise between SAS requirements and number of cells. The total number of mesh cells is about 1.50E+05 in 2D case and 2.20E+06 in 3D geometry, respectively. The 3D mesh is obtained extruding along the *z*-direction coordinate the bidimensional one. The boundary layer region is designed to obtain an initial $y^+ = 1$. The first cell height and the boundary layer thickness are computed adopting the flat plate solution approximation. Nodes around the hydrofoil profile are clustered approaching the surface wall, as well as the leading and trailing edge points. Nodes clustering distributions follow a hyperbolic spacing function. In the far field region, the grid node density increases moving towards the unstructured layer, both in the stream-wise and pitch-wise direction. No mesh clustering is instead applied in the span-wise direction.

a) *b)*

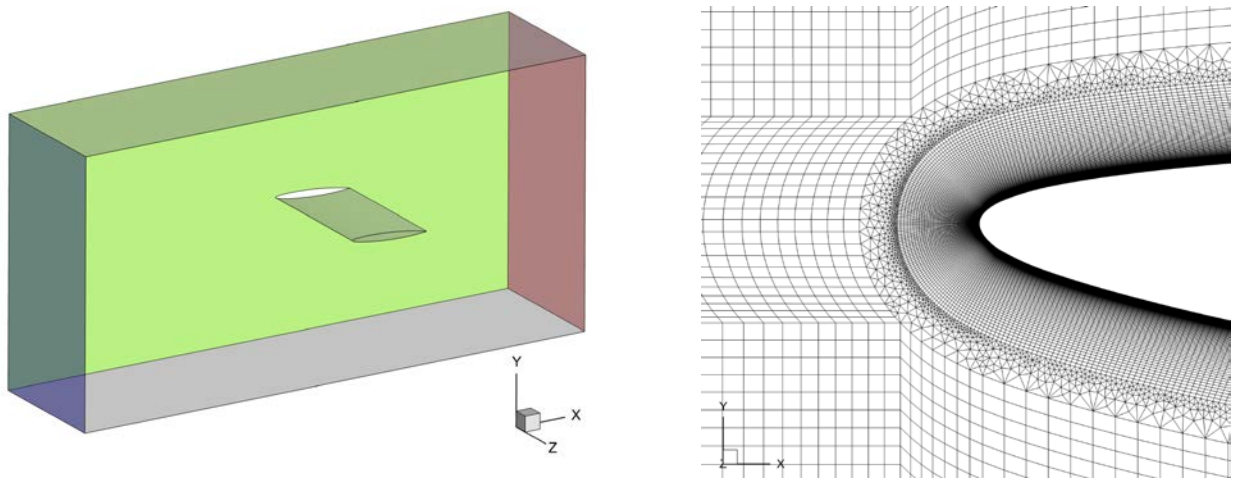

Fig.1: Computational domain description: *a)* 3D geometrical domain with coloured boundary conditions' surfaces; *b)* 2D mesh visualization in proximity of the hydrofoil leading edge, obtained on the central slice, *z* = 0.007 m.

RESULTS

According to the experimental data by Shen and Dimotakis (1989), pressure coefficients (eq. 15) are used as the main comparing parameter.

$$C_p(x) = \frac{p(x) - p_{ref}}{\frac{1}{2}\rho v_\infty^2} \tag{15}$$

Calculations are carried out using the Singhal cavitation model default coefficients. Firstly, for the $\sigma = 1.76$ case the behaviour of the TSST simulations were analysed by switching from a 2D to a 3D domain; then, for both the cavitating conditions, the comparison is made between the 3D stationary results with the time averaged SAS pressure coefficients. As SAS simulations are time dependent, averaged values are calculated in the time interval 0.05 s – 0.30 s in which the flow field

reached a semi-steady condition and turbulent fluctuations oscillate with a characteristic frequency. Plots reported in Fig. 2 show the pressure coefficients in the performed simulations for a cavitation number equal to 1.76: the horizontal axis represents the normalized curvilinear abscissa on the blade suction side, being $x/C = 0$ the leading edge of the hydrofoil, and $x/C = 1$ the trailing edge. As visible in Fig. 2a, no relevant variations of the pressure coefficients are found switching from a 2D to a 3D domain for the TSST steady case. In the other charts (Fig. 2b-d), deviations are observed between TSST and SAS results in the initial range $0.03 < x/C < 0.11$, in proximity of the region where cavitation occurs. Here TSST model seems to better reproduce the experimental behaviour of the pressure coefficient, while SAS exhibits the highest deviation respect to the first experimental point (0.43). The TSST computed pressure coefficient, instead, presents a maximum deviation of 0.17 for $x/C = 0.33$. This behaviour might be ascribed to the fact that the SAS simulation uses a standard SST k-ω model in the wall region which fails to correctly reproduce laminar to turbulent regime transition.

Despite a time-averaged evaluation is carried out for comparing steady and transient flow field results, turbulence influences deserve to be investigated taking into account the unsteady behaviour shown by temporal fluctuations close to the leading edge, where cavitation occurs. Oscillating time evolutions of pressure, x-velocity and vapour volume fraction are monitored in the period 0.05 s – 0.30 s (Fig. 3a, c). Evaluations are carried out on the middle plane, $z = 0.007$ m; in the absolute frame position x = 5.36E-01 m, y = 7.76E-04 m. The initial instant of the time assessments is chosen by dividing a reference length of 0.62 m, by the reference velocity magnitude, 12.36 m/s. The initial reference length guarantees a fully overcome of the NACA trailing edge.

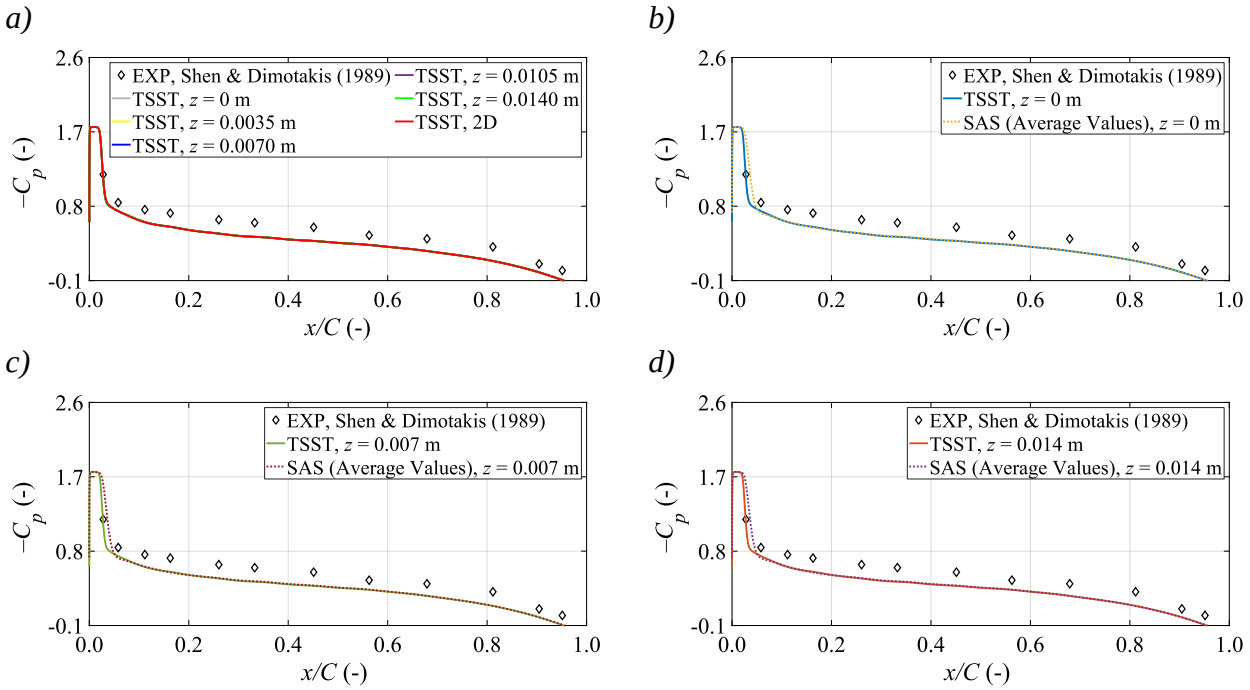

Fig. 2: Pressure coefficients comparisons with experiments, $\sigma = 1.76$: *a)* 2D and 3D TSST steady cases; *b)* TSST and SAS - time averaged (0.05 s < t < 0.30 s), $z = 0$ m; *c)* TSST and SAS - time averaged (0.05 s < t < 0.30 s), $z = 0.007$ m; *d)* TSST and SAS - time averaged (0.05 s < t < 0.30 s), $z = 0.014$ m.

A Fast Fourier Transformation (FFT) is adopted to assess the characteristic spectrum in the frequency domain. By analysing the frequency curve, it is possible to estimate the characteristic behaviour of the cavitation region on the hydrofoil suction side. FFT algorithms are performed

adopting a sampling time equal to the time step size, 3.62E-06 s for the current case. As expected, from the plots in Fig. 3b, 3d and 3f, pressure, *x*-velocity and vapour volume fractions FFT peaks are located at the same frequencies. Maximum peak frequencies are found at 8 Hz, corresponding to a characteristic time period of 0.12 s. Observing the temporal trends, this oscillating period is correlated to a long-time evolution, i.e., the temporal differences between two subsequent peaks oscillate with such higher frequency (~ 1.00E+02 Hz – 1.00E+03 Hz), as visible in the right part of the FFT spectra. Observing Fig. 3a, 3c, 3e, it is possible to link the long period behaviour to slow physical quantities fluctuations. FFTs representation is realized by removing the first peak, cantered at zero frequency. In researching the characteristic frequencies for the current time interval, in fact, an infinite period phenomenon doesn't produce any significant consideration.

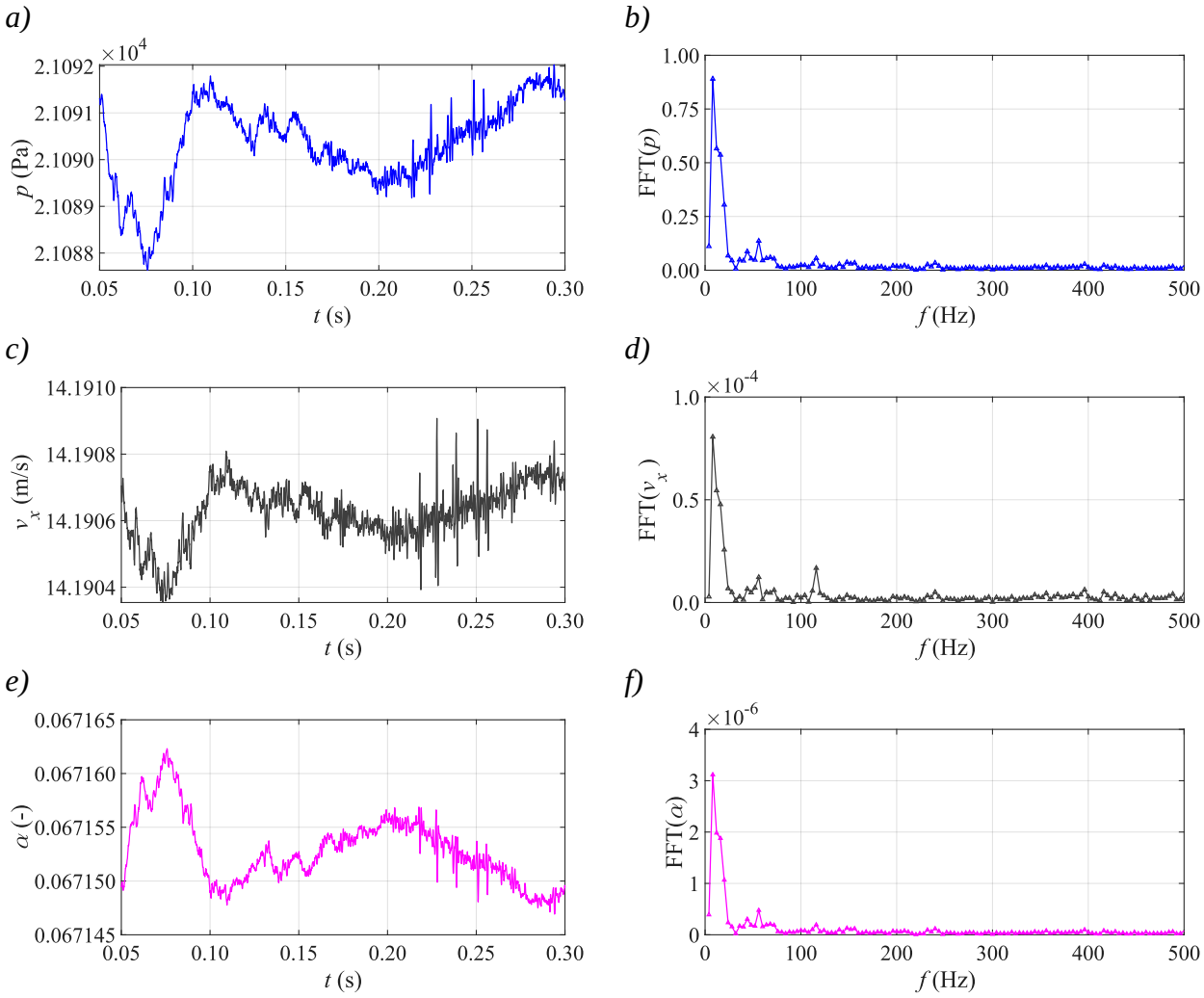

Fig. 3: SAS temporal trends and related FFTs computed on the coordinate point (*x* = 5.36E-01 m, *y* = 7.76E-04 m, *z* = 0.007 m), σ = 1.76: *a)* static pressure time evolution; *b)* static pressure FFT, *c)* *x*-velocity time evolution, *d)* *x*-velocity FFT, *e)* vapour volume fraction time evolution, *f)* vapour volume fraction FFT.

Following the methodology proposed by Yin et al. (a - c), the cavitating volume, V_C, temporal behavior is analyzed. Results are sampled each 200-time steps (7.24E-06 s). Time evolutions and related FFTs are reported in Fig. 4. Despite the different sampling time with respect to the charts of Fig. 3, in Fig. 4a it is possible to recognize an initial time variation whose extent is comparable to the

peak period of 0.12 s. Fig. 4b shows peak frequencies at 95 Hz and 155 Hz, meaning also in this case that the most relevant fluctuating modes are due to higher period oscillating phenomena. This can be observed from the wide variation of the curve in the left part of Fig. 4a.

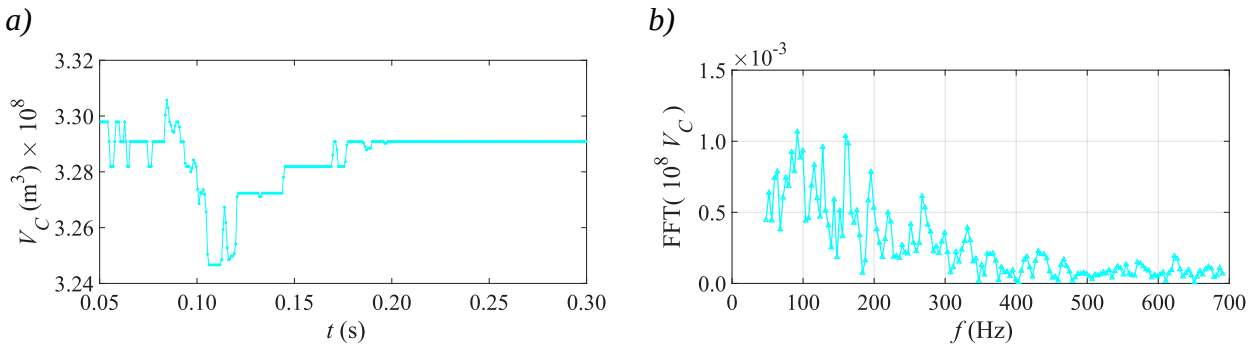

Fig. 4: SAS – cavity volume temporal trend and its FFT, σ = 1.76: *a)* cavity volume time evolution; *b)* cavity volume FFT.

The analyses previously shown are also performed for σ = 0.91. In Fig. 5a, pressure coefficients coming from the steady solution of the TSST – 3D simulation are compared for different z-coordinates. Despite a unique TSST behaviour is detected along the span-wise direction, the spatial trends differ from the experimental points, especially in the central part, 0.25 < x/C < 0.35. Maximum deviation of 0.61 is located at x/C = 0.33, the same position as in σ = 1.76 case (Fig. 2). As depicted in Fig. 5b-d the time averaged pressure coefficients computed from SAS simulation seems to better represent the experimental points till x/C = 0.26. Maximum deviation (0.67) is found at x/C = 0.33 in the middle plane, as visible in Fig. 5c. The pressure coefficient drop produces a deviation of 0.63 instead on the side planes, z = 0 m and z = 0.014 m, always for x/C = 0.33 (Fig. 5b and 5d). In the rear part of the hydrofoil TSST and SAS show a similar behaviour, well representing the experimental data in the abscissa ranges 0.4 – 0.6 and 0.9 – 1.0. Remarkable differences are instead detected in the range 0.6 – 0.9.

Time evolutions of static pressure, x-velocity and vapour volume fraction are reported Fig. 6. The elaborated FFTs are described by similar spectra with same peak frequency at 156 Hz. The corresponding peak period is equal to 6.41E-03 s. This FFT peak frequency is quite close to the minimum frequency computed between subsequent oscillating peaks (Fig. 6a, 6c, 6e). This means the most probable oscillating mode is located in the part of diagram in which peaks oscillate with the highest period.

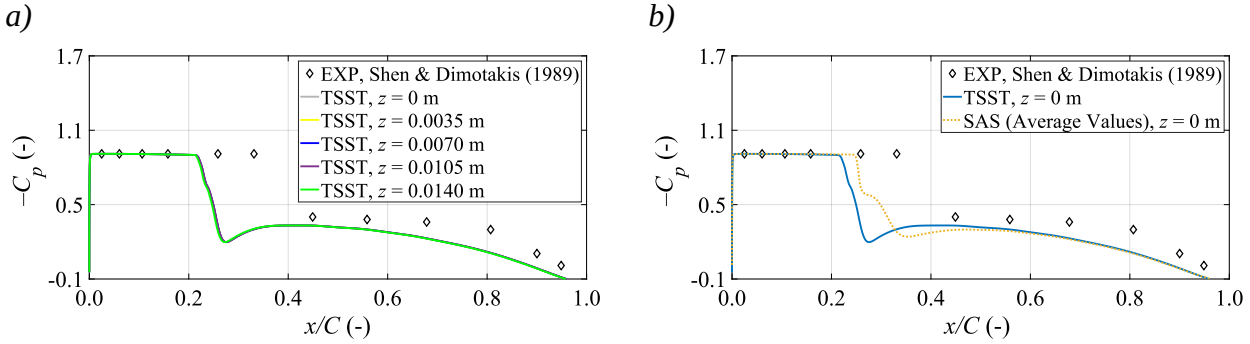

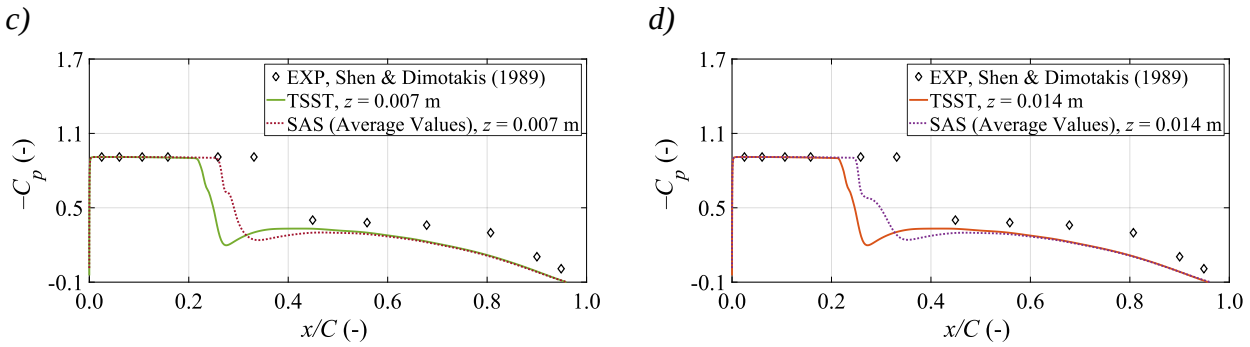

Fig. 5: Pressure coefficients comparisons with experiments, σ = 0.91: *a)* 3D TSST steady case; *b)* TSST and SAS - time averaged (0.05 s < *t* < 0.30 s), *z* = 0 m; *c)* TSST and SAS - time averaged (0.05 s < *t* < 0.30 s), *z* = 0.007 m; *d)* TSST and SAS - time averaged (0.05 s < *t* < 0.30 s), *z* = 0.014 m.

This zone is remarkable in the left part of the temporal trends, in the time interval of 0.05 s – 0.15 s where the crests are more rarefied. As previously stated, the first peak at zero frequency was removed, as physically meaningless.

Inspired by the previous works conducted by Yin et al. (a - c), cavity volume and related FFT spectrum are computed and then depicted in Fig. 7. Also in this case a different sampling period is adopted, 200 times the simulation time step size (7.08E-06 s). Despite the different time resolution, in Fig. 7b it is possible to recognize the 156 Hz peak, while the most probable oscillating mode is determined at 48 Hz. It physically means that a longer time period (2.08E-02 s) is strictly related with the conspicuous initial fluctuations.

The cavitating case described by σ = 1.76 reproduces a cavity volume two order of magnitude lower than the other, identified by σ = 0.91. To visualize the breathing mode of the cavitation cloud, the second cavitating case is chosen for a visual representation. In Fig. 8 we report four different instantaneous snapshots of the cavitating region.

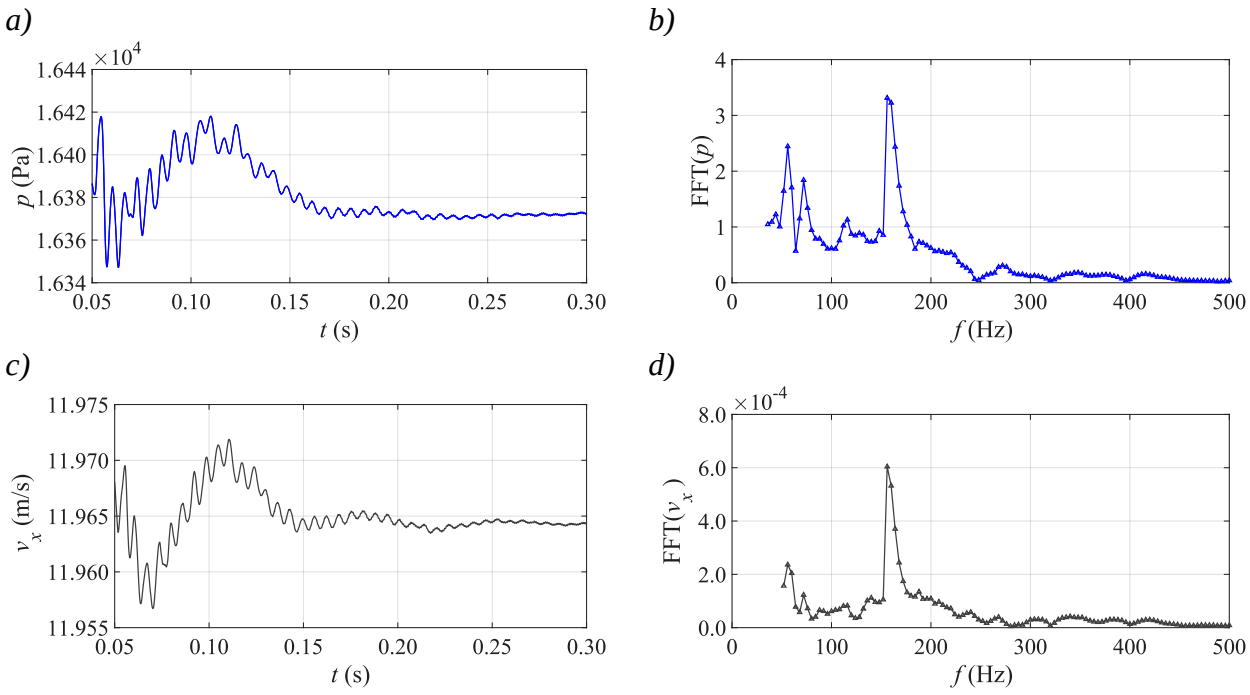

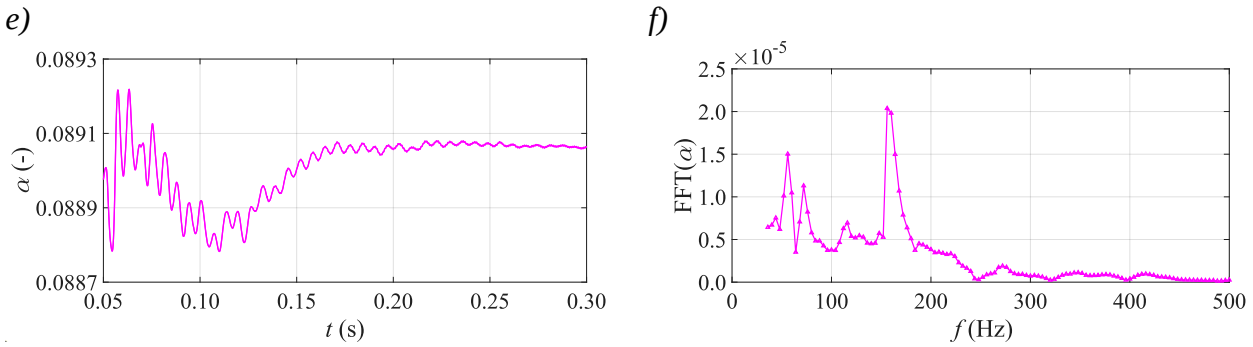

Fig. 6: SAS temporal trends and related FFTs computed on the coordinate point (*x* = 5.36E-01 m, *y* = 7.76E-04 m, *z* = 0.007 m), σ = 0.91: *a)* static pressure time evolution; *b)* static pressure FFT, *c)* *x*-velocity time evolution, *d)* *x*-velocity FFT, *e)* vapour volume fraction time evolution, *f)* vapour volume fraction FFT.

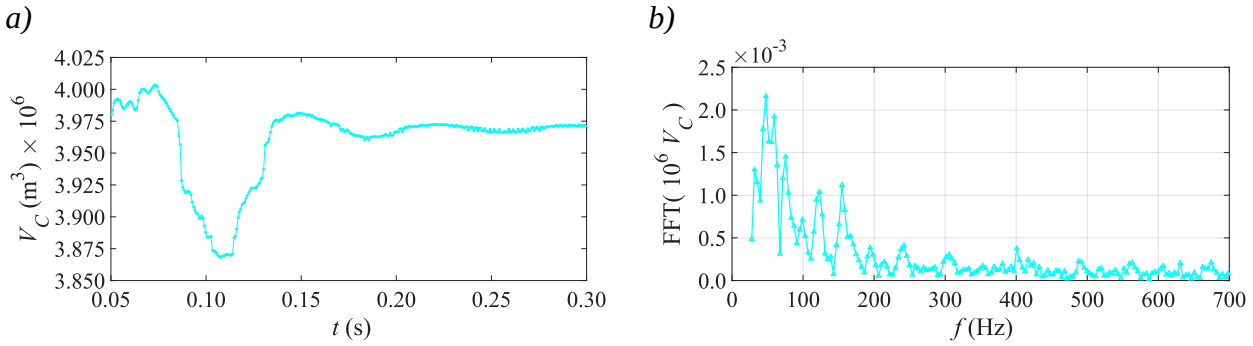

Fig. 7: SAS – cavity volume temporal trend and its FFT, σ = 0.91: *a)* cavity volume time evolution; *b)* cavity volume FFT.

Plots were made every 2.48E-02 s and show volume variations of the cavitation region induced by turbulence. As visible from the comparing dashed line position, Fig. 8b reports the contracted cavity instant with respect to the vapour volume fraction extent of Fig. 8a, 8c, 8d. The following instants (fig. 8c and 8d) represent a cavity recover, the extent of the vapour volume fraction at the right of the dashed line returns to grow, globally.

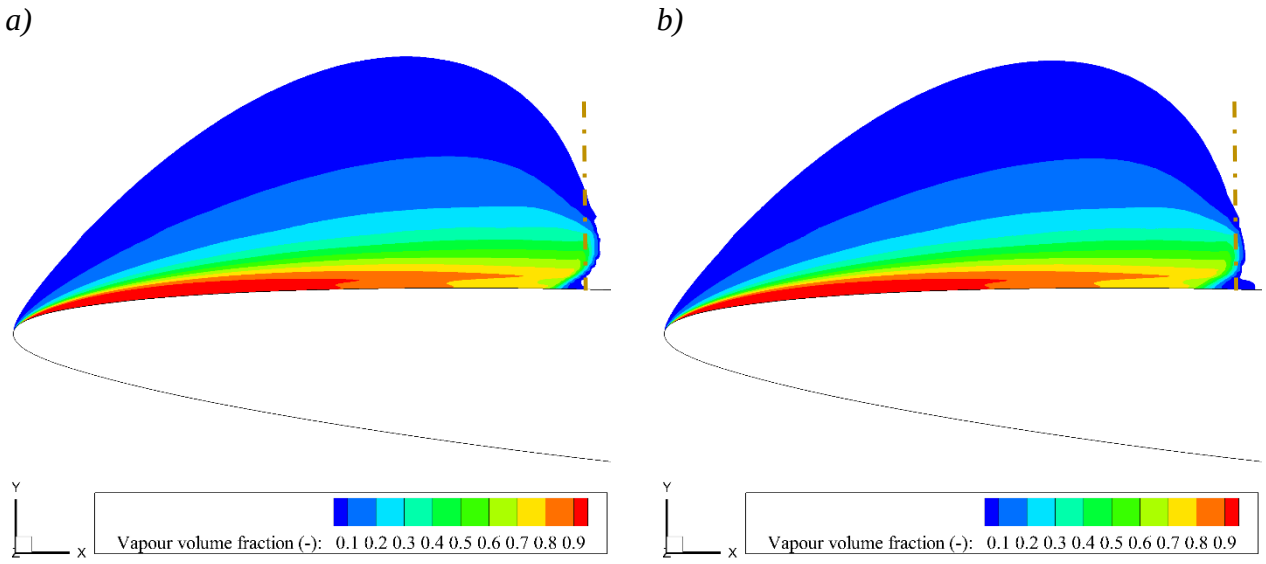

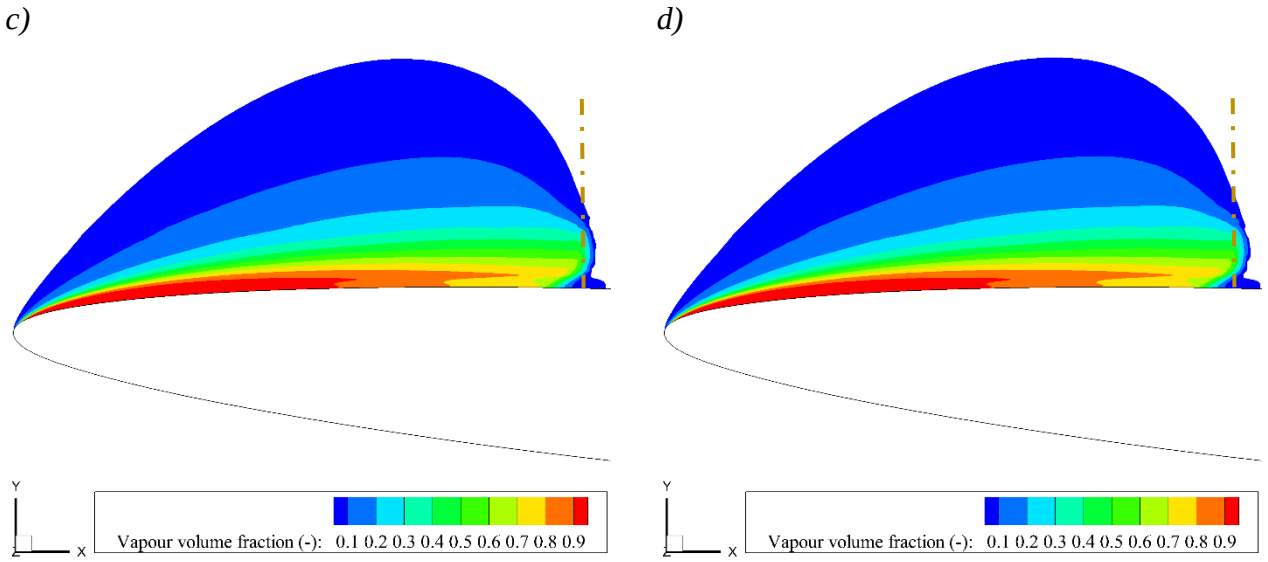

Fig. 8: Vapour volume fraction visualized on the middle plane (z = 0.007 m), with the representation of a dashed line for cavitation length comparison, σ = 0.91: *a)* SAS (t = 7.43E-02 s); *b)* SAS (t = 9.91E-02 s); *c)* SAS (t = 1.24E-01 s); *d)* SAS (t = 1.49E-01 s).

Noting the hydrofoil wall region, a lower vapour volume fraction zone develops (instants represented in Fig. 8b-d) at the right of the dashed line starting point.

CONCLUSIONS

For the higher cavitation number, no great differences are found between steady TSST simulations and SAS. In fact, when the Singhal model is adopted with default coefficients, pressure coefficients computed along the NACA 66 (MOD) hydrofoil are quite similar but in proximity of the cavitation region the TSST model provides results slightly closer to the experiments. Such a fact might be ascribed to the use of a standard SST k-ω model for SAS wall region treatment, which fails to correctly reproduce laminar to turbulent regime transition. By performing a FFT analysis, characteristic frequencies of the involved cavitation phenomenon were computed and the related periods are compared with the physical quantities' temporal trends. In this cavitating case the FFT peak frequency is equal to 8 Hz, leading to a macroscopic dominating oscillating mode, with respect to the highest-frequencies turbulent fluctuations. Cloud cavitation volume and related FFT spectrum are also computed and compered with the temporal and frequency considerations made.

The lower cavitation number highlights a SAS better representation of the pressure coefficients in the cavitating region with respect to the TSST model. Both the models differently interpret the rear part of the cavitation zone, $0.2 < x/C < 0.4$. Although from $x/C > 0.4$ they exhibit a similar behavior, substantial differences, respect to the experimental points distribution, are shown. Also in this case static pressure, x-velocity and vapour volume fraction are analyzed both in time and frequency domain, showing the most probable mode is due to the minimal oscillating frequency (156 Hz), encountered in the time range 0.05 s – 0.30 s. The cavitating cloud volume is plotted against time and its FFT is computed. Despite results are not sampled each time step, in the FFT spectrum a frequency peak, not the highest, of 156 Hz is always detectable. A major oscillating zone is singled out, confirming that, the lower frequencies dominate the evolutionary behavior in the analyzed time interval. Finally, a sequence of four snapshots of the vapour volume fraction is reported covering four

different time instants, distributed in the range 0.07 s – 0.15 s and highlighting the cavity breathing pulsations.

These aspects will be further analyzed by the authors in future works.

REFERENCES

Berntsen, G. S., Kjeldsen, M., Arndt, R. E., (2001). *Numerical modeling of sheet and tip vortex cavitation with FLUENT 5*. Proceedings of 4th International Symposium on Cavitation, Pasadena, United States of America

Bilus, I., Morgut, M., & Nobile, E., (2013). *Simulation of sheet and cloud cavitation with homogenous transport models*. International Journal of Simulation Modelling, 12, 94-106

Ducoin, A., Huang, B., & Young, Y. L. (2012). *Numerical modeling of unsteady cavitating flows around a stationary hydrofoil*. International Journal of Rotating Machinery, 2012, 1-17

Dular, M., Stoffel, B., Širok, B., (2006). *Development of a cavitation erosion model*. Wear, 261, 642-655

Ghahramani, E., Ström, H., Bensow, R. E., (2021). *Numerical simulation and analysis of multi-scale cavitating flows*. Journal of Fluid Mechanics, 922, 1-54

Gohil, P. P., Saini, R. P., (2014). *Coalesced effect of cavitation and silt erosion in hydro turbines—A review*. Renewable and Sustainable Energy Reviews, 33, 280-289

Hidalgo, V., Escaler, X., Valencia, E., Peng, X., Erazo, J., Puga, D., & Luo, X., (2019). *Scale-adaptive simulation of unsteady cavitation around a NACA66 hydrofoil*. Applied Sciences, 9, 1-11

Hong, S., Wu, Y., Wu, J., Zhang, Y., Zheng, Y., Li, J., Lin, J., (2021). *Microstructure and cavitation erosion behavior of HVOF sprayed ceramic-metal composite coatings for application in hydro-turbines*. Renewable Energy, 164, 1089-1099

Kozubková, M., Rautová, J., and Bojko, M., (2012). *Mathematical model of cavitation and modelling of fluid flow in cone*. Procedia Engineering, 39, 9-18

Kunz, R. F., Boger, D. A., Stinebring, D. R., Chyczewski, T. S., Lindau, J. W., Gibeling, H. J., Govindan, T. R. (2000). *A preconditioned Navier–Stokes method for two-phase flows with application to cavitation prediction*. Computers & Fluids, 29, 849-875

Kumar, P., & Saini, R. P., (2010). *Study of cavitation in hydro turbines - A review*. Renewable and Sustainable Energy Reviews, 14, 374-383

Lee, I., Park, S., Seok, W., Rhee, S. H., (2021). *A Study on the Cavitation Model for the Cavitating Flow Analysis around the Marine Propeller*. Mathematical Problems in Engineering, 2021, 1-8

Merkle, C. L., (1998). *Computational modelling of the dynamics of sheet cavitation*. Proceedings of the 3rd International Symposium on Cavitation, Grenoble, France

Menter, F. R., Egorov, Y. (2010). *The scale-adaptive simulation method for unsteady turbulent flow predictions. Part 1: theory and model description*. Flow, turbulence and combustion, 85, 113-138

Menter F. R., Langtry R. B., Likki S. R., Suzen Y. B., Huang P. G., and Volker S., (2004). *A Correlation-Based Transition Model Using Local Variables*. ASME Turbomachinery Journal, 128, 413-422

Morgut, M., Nobile, E., Biluš, I., (2011). *Comparison of mass transfer models for the numerical prediction of sheet cavitation around a hydrofoil*. International Journal of Multiphase Flow, 37, 620-626

Olsson M., (2008). *Numerical investigation on the cavitating flow in a waterjet pump*. Department of Applied Mechanics, Division of Fluid Dynamics, Chalmers, University of Technology, Göteborg, Sweden, Thesis - 44, 1-69

Saito, Y., Takami, R., Nakamori, I., Ikohagi, T., (2007). *Numerical analysis of unsteady behavior of cloud cavitation around a NACA0015 foil*. Computational Mechanics, 40, 85-96

Savio, A., Cianferra, M., Armenio, V., (2021). *Analysis of Performance of Cavitation Models with Analytically Calculated Coefficients. Energies*, 14, 1-22

Schnerr, G. H., Sauer, J., (2001). *Physical and numerical modeling of unsteady cavitation dynamics*. Proceedings of 4th International Conference on Multiphase Flow, New Orleans

Senocak, I., Shyy, W., (2002). *Evaluations of cavitation models for Navier-Stokes computations*. In Fluids Engineering Division Summer Meeting, 36150, 395-401

Singhal, A. K., Athavale, M. M., Li, H., Jiang, Y., (2002). *Mathematical basis and validation of the full cavitation model*. J. Fluids Eng., 124, 617-624

Shen, Y., Dimotakis, P. E., (1989). *The influence of surface cavitation on hydrodynamic forces*. Proceedings of the 22nd American towing tank conference, St. John's, Newfoundland, Canada

Tseng, C. C., Wang, L. J., (2014). *Investigations of empirical coefficients of cavitation and turbulence model through steady and unsteady turbulent cavitating flows*. Computers & Fluids, 103, 262-274

Wang, G., Senocak, I., Shyy, W., Ikohagi, T., Cao, S., (2001). *Dynamics of attached turbulent cavitating flows*. Progress in Aerospace sciences, 37, 551-581

Yin, T., Pavesi, G., Pei, J., Yuan, S., (2021, a). *Numerical investigation of unsteady cavitation around a twisted hydrofoil*. International Journal of Multiphase Flow, 135, 103506

Yin, T., Pavesi, G., Pei, J., Yuan, S., (2022, b). *Numerical investigation on the inhibition mechanisms of unsteady cavitating flow around stepped hydrofoils*. Ocean Engineering, 265, 112540

Yin, T., Pavesi, G., Pei, J., Yuan, S., (2021, c). *Numerical analysis of unsteady cloud cavitating flow around a 3d clark-y hydrofoil considering end-wall effects*. Ocean Engineering, 219, 108369

Young, F. R., (1999). *Cavitation*. Imperial Collage Press, England

Zwart, P. J., Gerber, A. G., Belamri, T., (2004). *A two-phase flow model for predicting cavitation dynamics*. Proceedings of 5th International Conference on Multiphase Flow, Yokohama, Japan

